SuperGaussians: Enhancing Gaussian Splatting Using Primitives with Spatially Varying Colors

Rui Xu[1], Wenyue Chen[2], Jiepeng Wang[1], Yuan Liu[3,4†]
Peng Wang[1], Lin Gao[5], Shiqing Xin[6], Taku Komura[1], Xin Li[7], Wenping Wang[7†]

[1]The University of Hong Kong   [2]Dalian University of Technology   [3]Nanyang Technological University
[4]HKUST   [5]Chinese Academy of Sciences   [6]Shandong University   [7]Texas A&M University

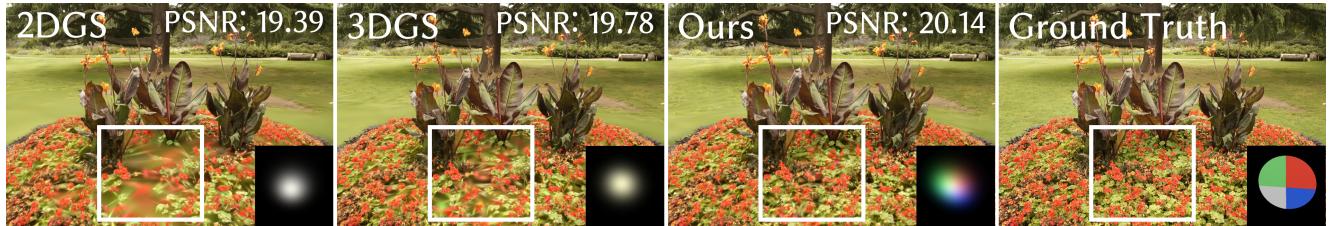[†] Corresponding authors.   https://ruixu.me/html/SuperGaussians/index.html

Figure 1. SuperGaussians gives each Gaussian the ability to vary spatially. Compared with 2DGS [11] and 3DGS [16], SuperGaussians is more expressive and can better reconstruct details (as seen in the white area). Additionally, SuperGaussians can express more color variations using only one Gaussian, instead of being limited to just one color (bottom right).

Abstract

*Gaussian Splattings [11, 16] demonstrate impressive results in multi-view reconstruction based on Gaussian explicit representations. However, the current Gaussian primitives only have a single view-dependent color and an opacity to represent the appearance and geometry of the scene, resulting in a non-compact representation. In this paper, we introduce a new method called **SuperGaussians** that utilizes spatially varying colors and opacity in a single Gaussian primitive to improve its representation ability. We have implemented bilinear interpolation, movable kernels, and even tiny neural networks as spatially varying functions. Quantitative and qualitative experimental results demonstrate that all three functions outperform the baseline, with the best movable kernels achieving superior novel view synthesis performance on multiple datasets, highlighting the strong potential of spatially varying functions. Our code can be found at: https://github.com/Xrvitd/SuperGaussians.*

1. Introduction

Novel-view synthesis (NVS) has always been an important task in computer graphics and computer vision, with various applications in robotics, AR/VR, and autonomous driving. Compared with neural radiance fields (NeRF) [22]-based methods, recent Gaussian splatting methods [11, 16] directly reconstruct 3D scenes by splatting explicit Gaussian primitives like ellipsoids [16] or surfels [11], achieving significant progress in novel view synthesis and geometric reconstruction.

Though impressive NVS quality has been achieved by these Gaussian splatting-based methods, these methods are ineffective and non-compact in representing a complex scene. In these methods, the input images are fitted by splatting a set of Gaussian primitives. Each primitive only has a single view-dependent color and an opacity to represent the appearance and geometry of the scene. However, when the scene has complex geometry and appearance, these methods have to create a large number of these simple Gaussians to approximate the spatially varying opacity and textures on the scene, which leads to a huge waste of Gaussians. An example is shown in the right bottom of Fig. 1, where our target is to fit a round plane with four different colors, while the original 2DGS [11] or 3DGS [16] all fail to reconstruct the colors and opacity of this simple shape by using one Gaussian primitive.

To address this problem, we introduce a new method called **SuperGaussians** that utilizes spatially varying colors and opacity in a single Gaussian primitive to improve

its representation ability. This spatially varying attribute means that different rays that intersect the same Gaussian primitive may have different colors if these rays intersect the Gaussian at different locations. In the vanilla Gaussian Splatting, Gaussian primitives always have the same opacity or view-dependent colors for all rays while our spatially varying Gaussians show different colors for different intersection points. This makes a single Gaussian more capable of fitting complex textures and geometry in the scene, increasing representation ability and making our representation more compact and effective, as shown in Fig. 1.

To define the spatially varying function inside a Gaussian primitive, we try three different designs. As shown in Fig. 2, all three spatially varying functions are implemented based on Gaussian surfels [11]. The first function divides each Gaussian surfel into four quadrants using bilinear interpolation, assigning a learnable color and opacity value to each quadrant, which enhances color expression but may cause gradient vanishing issues (See Fig. 3 (a)). In the second design, we define four movable kernels based on the original Gaussian surfel, providing higher flexibility and stronger expressiveness, as shown in Fig. 3 (b). Third, we apply a tiny three-layer neural network on each Gaussian surfel that can return a color and opacity value for any intersection point on the surfel. Such neural network-based representation shows strong representation ability but with significantly more parameters than the other two functions.

To demonstrate the effectiveness of SuperGaussians, we conduct experiments on the Synthetic Blender [22], DTU [13], Mip-NeRF360 [3], and Tanks&Temples [17] datasets to validate all three designs. Experimental results demonstrate that all three spatially varying functions outperform the baseline method 2DGS [11] in novel view synthesis, while the compact movable kernels design achieves the best results. Moreover, SuperGaussians with movable kernels surpasses all other Gaussian Splatting-based methods on almost all datasets. We further demonstrate the compactness of SuperGaussians by using a limited number of Gaussian primitives to achieve superior rendering quality.

2. Related Works

3D reconstruction has been widely studied in the past. Different from reconstructing geometric models from point clouds [15, 19, 23, 29, 30], reconstructing images [16, 22, 25, 27] and shapes [9, 11, 28] from multi-view images has always been a harder problem to be solved.

2.1. Novel View Synthesis

Seitz et al. [27] introduces multi-view stereo (MVS) reconstruction algorithms that determine per-view depth maps by maximizing multi-view consistency through patch or feature-level matching, followed by surface reconstruction via multi-view fusion. Subsequent methods like COLMAP [26], OpenMVS [24], and PMVS [8] excel on texture-rich, flat surfaces but struggle in textureless areas and near occlusion boundaries. Recently, learning-based MVS approaches, such as MVSNet [31] and its variants [21, 32, 34, 36], have mitigated the issues in textureless regions, but suffer from lack of multi-view consistency due to the independent depth prediction for each view. Schonberger and Frahm [25] proposes a incremental Structure-from-Motion (SfM) technique that addresses key challenges in robustness, accuracy, completeness, and scalability. The famous NeRF [22] and its variants [1, 2, 4, 12] presents a method that achieves remarkable results in synthesizing novel views of complex scenes by optimizing a continuous volumetric scene function with a sparse set of input views using a fully connected deep network, effectively rendering photorealistic images through differentiable volume rendering.

2.2. Gaussian-based methods.

Recently, 3DGS [16] achieves impressive visual quality and real-time novel-view synthesis by using 3D Gaussians for scene representation, interleaved optimization of anisotropic covariance, and a fast visibility-aware rendering algorithm, demonstrating superior results on several established datasets.

Due to the excellent explicit expression ability of 3DGS [16], many methods based on Gaussian splatting have been proposed. Scaffold-GS [20] uses anchor points to distribute local 3D Gaussians and dynamically predicts their attributes based on viewing direction and distance, reducing redundant Gaussians and improving scene coverage, thereby enhancing rendering quality. Mip-splatting [35] introduces a 3D smoothing filter to constrain the size of 3D Gaussian primitives and a 2D Mip filter to mitigate aliasing and dilation issues, demonstrating effectiveness across multiple scales. GES [10] improves 3D scene representation efficiency and accuracy over Gaussian Splatting by using fewer particles and a frequency-modulated loss, significantly reducing memory footprint and increasing rendering speed. 3D-HGS [18] addresses the limitations of 3DGS [16] in representing discontinuous functions, demonstrating improved performance and rendering quality without compromising speed. PixelSplat [6] introduces a feed-forward model that reconstructs 3D radiance fields from image pairs using 3D Gaussian primitives, achieving significantly faster 3D reconstruction on novel view synthesis. Following 3DGS [16], 2DGS [11] and Gaussian Surfels [7] was proposed by compressing the ellipsoid into a Gaussian surfel by defining the shortest axis of the ellipsoid as the normal vector, achieving high-quality geometric reconstruction while retaining the ability to reconstruct from novel views.
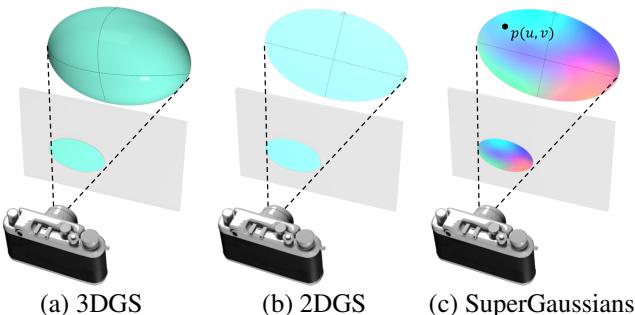
(a) 3DGS   (b) 2DGS   (c) SuperGaussians

Figure 2. 3DGS [16] uses Gaussian ellipsoids to express scenes, and a learnable color is defined on each ellipsoid. 2DGS [11] uses Gaussian surfels to express scenes, and a learnable color is defined on each Gaussian surfel. Our SuperGaussians uses spatially varying Gaussian surfels to express scenes, and the color and opacity changes with the spatial position on each surfel.

(a) Bilinear Interpolation   (b) Movable kernels

(c) Bilinear Interpolation   (d) Movable kernels

Figure 3. Visualization of the bilinear interpolation (a,c) and movable kernel functions (b,d).

3. Method

3.1. Spatially Varying Gaussian Primitives

Gaussian Splattings. Given multi-view images with the corresponding camera poses, our target is to render novel-view images. We achieve this by representing the whole scene with a set of trainable Gaussian primitives. Then, to train these parameters of all Gaussian primitives, we apply the splatting technique to render images on the input viewpoints and minimize the difference between the rendered images and input images. After learning the Gaussian primitives, we can apply the same splatting technique to render images of arbitrary viewpoints.

Colors and Opacity of Gaussian Primitives. The colors and opacity of Gaussian primitives in existing methods [11, 16, 18, 35] are independent of the intersection locations with the primitives, which leads to ineffective representation ability for complex textures or geometry in a complex scene. The colors are usually represented by a view-dependent spherical harmonic function $\mathbf{c}(\mathbf{d}) = SH(\mathbf{d})$, where $\mathbf{d}$ is the viewing direction and SH means the spherical harmonic function. The opacity α is a single value associated with the Gaussian primitive. To render an image, we perform alpha-blending [38] using the colors and opacity of these Gaussian primitives. A noticeable issue is that the Gaussian primitives show exactly the same color for different rays with the same viewing direction but intersect this primitive with different intersection points. Utilizing such simple color function forces to represent an underlying surface with complex textures leads to ineffective and redundant small Gaussian primitives. The same issue also exists for the opacity, which only monotonously decreases with the Gaussian function and thus has difficulty in representing complex geometry.
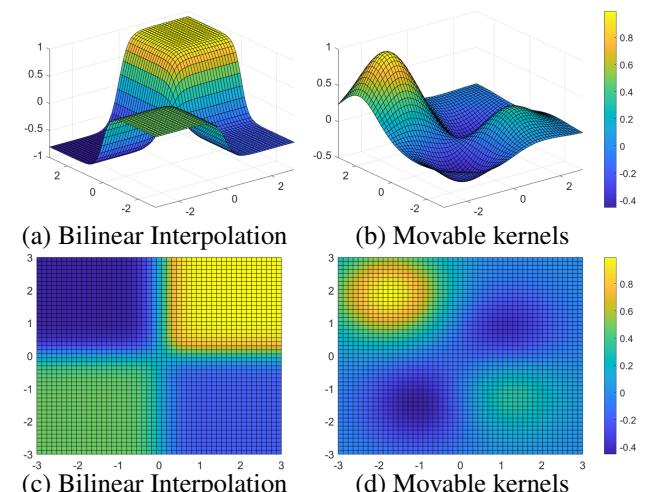
Spatially Varying Colors and Opacity. To address the above issue, we propose spatially varying colors and opacity in SuperGaussians. Specifically, we use a color function $\mathbf{c}(\mathbf{p}, \mathbf{d})$ and an opacity function $\alpha(\mathbf{p})$ as

$$\mathbf{c}(\mathbf{p}, \mathbf{d}) = SH(\mathbf{d}) + \mathcal{F}_{\mathbf{c}}(\mathbf{p}), \qquad (1)$$

$$\alpha(\mathbf{p}) = \mathcal{F}_{\alpha}(\mathbf{p}), \qquad (2)$$

where $\mathbf{p}$ is the intersection point between the given Gaussian primitive and the ray from current pixel. By defining the opacity and colors with these two spatially varying functions, we greatly improve the representation ability and make the Gaussian primitives more effective for complex textures and geometry. Note that we do not pose any constraints on the values of $\mathcal{F}_{\mathbf{c}}$ and $\mathcal{F}_{\alpha}$ so these functions could be negative. Thus, recent works like 3D-HGS [18] and NegGS [14] are special cases of our SuperGaussians.

Computation of Intersection Point $\mathbf{p}$. To compute an intersection point for our method, we adopt the 2D Gaussian Splatting [11] to use surfels as the Gaussian primitives. Then, the intersection point $\mathbf{p}$ is defined as the intersection point on the Gaussian surfel $\mathbf{p} = (u, v)$. Note that we use 2DGS by default for simplicity, but our discussion can also be extended to 3D Gaussians by regarding the 3D Gaussians as ellipsoids and using the intersection points with the ellipsoids, while the calculation of intersection points requires careful consideration. In the following, we discuss three different implementations of our spatially varying functions $\mathcal{F}_{\mathbf{c}}$ and $\mathcal{F}_{\alpha}$.

3.2. Bilinear Interpolation

In this function, we use bilinear interpolation to divide each elliptical Gaussian into four quadrants, where each quadrant has different color and opacity values. Then calculate

3

Figure 4. The parameter amounts of the three proposed spatial variation functions and the original 2DGS [11] on a single Gaussian. The parameter amounts of the three proposed functions are 1.28 times, 1.40 times, and 1.88 times of the original 2DGS [11].

$\mathbf{c}(\mathbf{p}, \mathbf{d})$ and $\alpha(\mathbf{p})$ at any position in object space through bilinear interpolation.

The bilinear interpolated color can be obtained by a simple bilinear interpolation

$$\mathcal{F}_\mathbf{c}(\mathbf{p}) = (1 - u')(1 - v')\mathbf{c}_0 + (1 - u')v'\mathbf{c}_1 \\ + u'(1 - v')\mathbf{c}_2 + u'v'\mathbf{c}_3, \quad (3)$$

and the same goes for opacity

$$\mathcal{F}_\alpha(\mathbf{p}) = (1 - u')(1 - v')\alpha_0 + (1 - u')v'\alpha_1 \\ + u'(1 - v')\alpha_2 + u'v'\alpha_3, \quad (4)$$

where $\mathbf{c}_i$ and α_i for $i = 0, 1, 2, 3$ are the four new learnable colors and opacities corresponding to the four quadrants. We also use a simple sigmoid function to rescale the coordinates $\mathbf{p} = (u, v)$ in the object space to $(0, 1)$ to avoid some irregular values:

$$u' = \frac{1}{1 + e^{-\lambda_s u}}, \quad v' = \frac{1}{1 + e^{-\lambda_s v}}, \quad (5)$$

where λ_s is a learnable parameter that controls the changing rate of the sigmoid function. We set it to 5.0 by default and allow it to change with the gradient during optimization.

3.3. Movable kernels

The above bilinear interpolation method can be regarded as four fixed kernels located in the four quadrants of the elliptical Gaussian surfel. This inspires us to further enhance its expressiveness by using movable kernels.

We define k movable kernels $\mathbf{K}_i = (K_i^x, K_i^y)$ on each Gaussian surfel, where $i = 0, 1, 2, \ldots, k - 1$ corresponds to the index of kernels. Assume that the intersection point of the current pixel and Gaussian surfel is $\mathbf{p} = (u, v)$. The color and opacity can be calculated by:

$$\mathcal{F}_\mathbf{c} = \sum_{i=0}^{k-1} \mathcal{F}_{\mathbf{K}_i}(\mathbf{p})\mathbf{c}_i, \\ \mathcal{F}_\alpha = \sum_{i=0}^{k-1} \mathcal{F}_{\mathbf{K}_i}(\mathbf{p})\alpha_i, \quad (6)$$

In our implementation, each kernel is represented as a separate exponential function that decays as the distance from the point $\mathbf{p}$ to the kernel center $\mathbf{K}_i$

$$\mathcal{F}_{\mathbf{K}_i}(\mathbf{p}) = e^{-\lambda_e \|\mathbf{p} - \mathbf{K}_i\|^2}, \quad (7)$$

where λ_e is similar to the λ_s mentioned in the previous section, both of which are used to control the changing rate of the kernel function. We set $\lambda_e = 0.1$ and $k = 4$ by default. Fig. 3 demonstrates the numerical visualizations of these two spatially varying functions, and we can also choose other kernel functions like the sigmoid function as introduced in Sec. 4.

3.4. Tiny MLPs

Instead of using an interpolation or kernel function to represent the spatially varying function, we define a separate small multilayer perceptron (MLP) on each Gaussian surfel. To reduce the number of parameters as much as possible, we only use a three-layer MLP as the spatial variation function

$$\mathcal{F}_\mathbf{c}, \mathcal{F}_\alpha = \text{MLP}(\mathbf{p}), \quad (8)$$

where the MLP accepts a two-dimensional input $\mathbf{p} = (u, v)$ and outputs the color and opacity at that location, as shown in the wrapped figure. Inside the MLP, we adopt the sigmoid function is used as the activation function. However, although we adopt a shallow three-layer MLP, the number of parameters still far exceeds the other two functions, as shown in Fig. 4.

4. Experimental Results

4.1. Implementation

SuperGaussians is implemented based on the 2DGS [11] code framework. We modified their CUDA kernels to implement our method and derived the corresponding backpropagation gradient code for each different spatially varying function. We followed all the setting parameters of 2DGS [11] and 3DGS [16] and compared them under the same conditions. As used in 2DGS [11] and 3DGS [16], we trained for 30K iterations while keeping the gradient splitting threshold at 0.0002, resetting the opacity to 0.01 every 3000 iterations, and stopping the splitting, cloning and removing of Gaussians after 15K iterations. We discard the normal consistency loss because we only focus on the quality of novel view synthesis. All our experiments were run on a single NVIDIA A100 80GB GPU and an Intel(R) Xeon(R) Platinum 8375C CPU.

Dataset	Synthetic Blender						Mip-NeRF360						Tanks&Temples						DTU					
GS Num	50K			noLimit			500K			noLimit			500K			noLimit			100K			noLimit		
Metrics	PSNR	SSIM	LPIPS	PSNR	SSIM	LPIPS	PSNR	SSIM	LPIPS	PSNR	SSIM	LPIPS	PSNR	SSIM	LPIPS	PSNR	SSIM	LPIPS	PSNR	SSIM	LPIPS	PSNR	SSIM	LPIPS
2DGS	32.64	0.963	0.042	32.87	0.965	0.038	25.93	0.755	0.314	26.86	0.796	0.255	22.63	0.821	0.231	23.19	0.830	0.214	32.25	0.922	0.196	34.43	0.939	0.169
2DGS*	32.89	0.965	0.039	33.13	0.968	0.031	26.27	0.765	0.301	27.01	0.816	0.208	22.88	0.824	0.223	23.07	0.836	0.189	32.74	0.932	0.181	34.69	0.950	0.131
Ours-BI	33.08	0.965	0.040	33.69	0.969	0.031	26.31	0.756	0.300	26.75	0.796	0.233	23.49	0.833	0.211	23.75	0.837	0.197	34.34	0.933	0.176	37.11	0.950	0.137
Ours-NN	33.15	0.966	0.039	33.39	0.968	0.036	26.44	0.762	0.305	26.92	0.795	0.258	23.17	0.829	0.222	23.26	0.830	0.216	33.88	0.929	0.201	34.7	0.935	0.187
Ours-MK	33.09	0.965	0.040	34.10	0.970	0.030	26.55	0.767	0.293	27.31	0.815	0.209	23.28	0.831	0.209	23.72	0.847	0.179	34.29	0.935	0.174	37.76	0.957	0.117

Table 1. Comparisons of three different spatially varying functions and the original 2DGS [11] with different number limits. For a fairer comparison, we provide 2DGS*, which uses the same total number of parameters as our movable kernel method by increasing the number of points. This table shows the PSNR on the Synthetic Blender dataset [22], Mip-NeRF360 [3] dataset, Tanks&Temples [17] dataset, and DTU [13] dataset. The top three results are highlighted in red, orange, and yellow, respectively.

Metrics	Synthetic Blender			Mip-NeRF360			Tanks&Temples		
	PSNR	SSIM	LPIPS	PSNR	SSIM	LPIPS	PSNR	SSIM	LPIPS
Plenoxels	31.76	-	-	23.08	0.626	0.463	21.08	0.719	0.379
INGP-Base	33.18	-	-	25.30	0.671	0.371	21.72	0.723	0.330
Mip-NeRF360	33.09	-	-	27.69	0.792	0.237	22.22	0.759	0.257
3DGS	33.32	-	-	27.21	0.815	0.214	23.14	0.841	0.183
2DGS	32.87	0.965	0.038	26.86	0.796	0.255	23.19	0.830	0.214
Ours-MK	34.10	0.970	0.030	27.31	0.815	0.209	23.72	0.847	0.179

Table 2. PSNR on Synthetic Blender [22], Mip-NeRF360 [3] and Tanks&Temples [17] datasets. Note that all data except 2DGS [11] are from the 3DGS paper.

	PSNR↑	SSIM↑	LPIPS↓
2DGS	34.43	0.939	0.169
Ours-MK	37.76	0.957	0.117

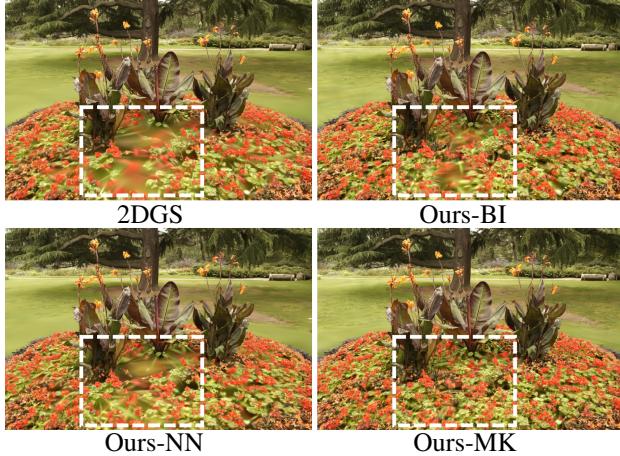Table 3. Novel View Synthesis comparison with 2DGS [11] on the DTU [13] dataset.

2DGS   Ours-BI

Ours-NN   Ours-MK

Figure 5. Visual comparison between three different spatially varying functions and 2DGS [11].
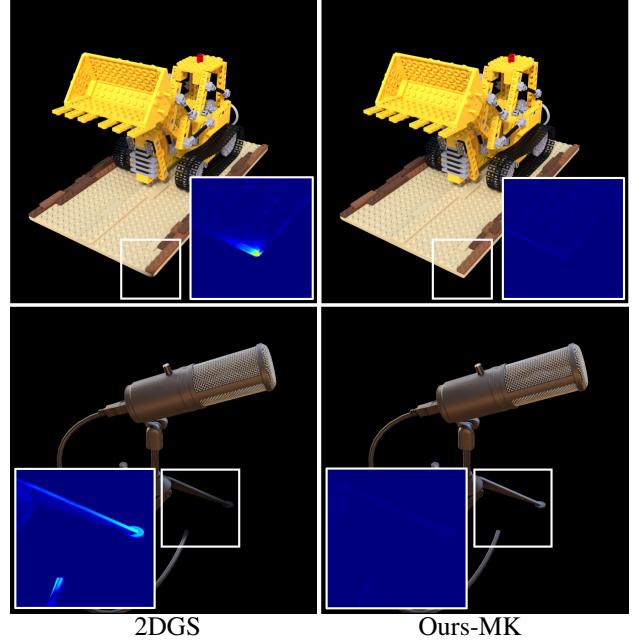

2DGS   Ours-MK

Figure 6. Visualization comparison with 2DGS [11] on the Synthetic Blender [22] dataset. The blue zoom-in windows show the error map against the ground truth image.

4.2. Comparison

Dataset. We tested our method on multiple datasets, including Synthetic Blender [22], DTU [13], Mip-NeRF360 [3], and Tanks&Temples [17], and we follow the same evaluation settings of 2DGS [11] and 3DGS [16] including the image resolution and the choice test set. We use PSNR, SSIM [5], and LPIPS [37] to measure the performance on all datasets for the novel-view-synthesis task. For the surface reconstruction, use Chamfer Distance (CD) to measure the accuracy of geometry on the DTU [13] dataset.

Comparison on Different Spatially Varying Functions. First, we present the comparison between 2DGS [11] and three of our spatially varying functions in Table 1. For per-scene results, please refer to the supplementary material. To avoid errors caused by different numbers of Gaussian points and to further demonstrate our stronger expressiveness, we also tested different functions and the original 2DGS [11] with a limited number of Gaussians, as shown in Table 1.

For a fair comparison, we provide 2DGS*, which uses the same total number of parameters as our movable kernel method by increasing the number of Gaussian primitives, and they are not following the number limit in the table. It can be seen that on most datasets, our movable kernel achieves the best reconstruction quality for the novel-view-synthesis task. The spatially varying function of bilinear in-
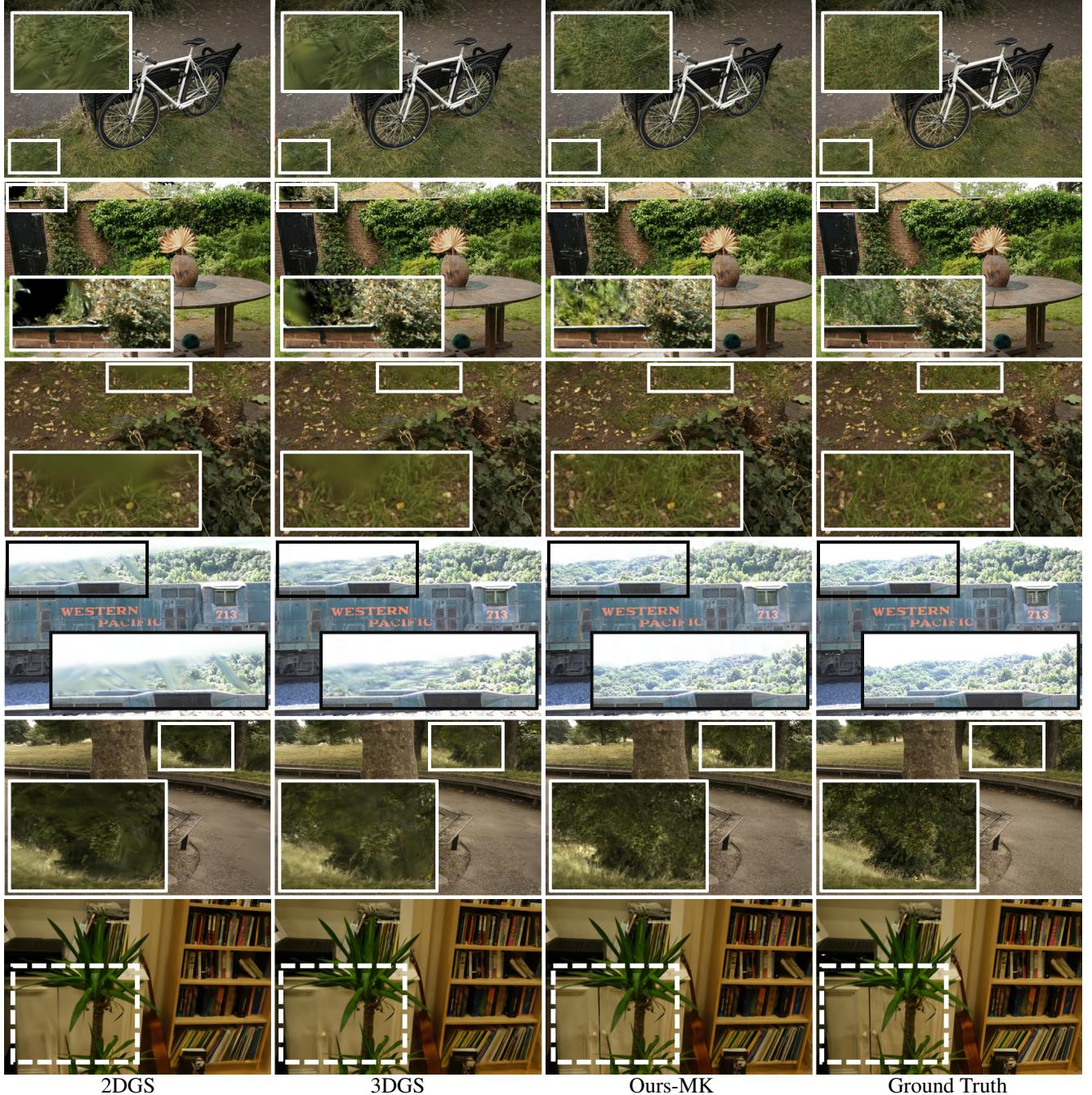
5

Figure 7. Visual comparison with 2DGS [11] and 3DGS [16] on both the Mip-NeRF360 [3] dataset and the Tanks&Temples [17] dataset shows that SuperGaussians can reconstruct details better due to stronger expressiveness.

2DGS	3DGS	Ours-MK	Ground Truth

terpolation also achieves good results in some of the scenes. The tiny neural network performs well when the number of Gaussian primitive is limited, demonstrating its strong representation ability. However, optimizing a neural network is usually difficult with unstable convergence, thus performing worse than the other two functions without limiting primitive numbers.

Additionally, the spatially varying functions based on

bilinear interpolation and tiny neural networks surpassed 2DGS [11], proving the effectiveness of these spatially varying functions. Fig. 5 shows the visual comparison of these three spatially varying functions. It can be seen that although the movable kernel function does not have the largest number of parameters (as shown in Fig. 4), it has the best ability to reconstruct details. While the other two spatially varying functions cannot reconstruct all details as

Nums	50K		100K		noLimit	
Metrics	CD↓	PSNR↑	CD↓	PSNR↑	CD↓	PSNR↑
2DGS	1.11	28.76	0.84	32.25	0.75	34.43
Ours	0.99	29.86	0.82	32.80	0.76	35.22

Table 4. Chamfer distance and PSNR comparison of geometric reconstruction on the DTU [13] dataset, we use the normal consistency loss provided by 2DGS [11] in this table.

	PSNR↑	SSIM↑	LPIPS↓
2DGS-w.$\mathcal{L}_N$	32.87	0.965	0.038
2DGS-w/o.$\mathcal{L}_N$	33.65	0.969	0.034
Ours-w.$\mathcal{L}_N$	33.85	0.970	0.031
Ours-w/o.$\mathcal{L}_N$	34.10	0.970	0.030

Table 5. Ablation on the normal consistency loss, we present the comparative results of 2DGS [11] and our method on the Synthetic Blender dataset [22] dataset, both with and without normal loss.

	PSNR↑	SSIM↑	LPIPS↓	GS Num↓
2DGS-Grad	32.58	0.957	0.038	446K
2DGS-Split	32.65	0.959	0.038	392K
2DGS†-Grad	34.05	0.970	0.028	387K
2DGS†-Split	33.94	0.970	0.029	384K
Ours-MK	34.10	0.970	0.030	205K

Table 6. Compared with 2DGS [11], which has more Gaussian points on the Synthetic Blender dataset [22], "Grad" indicates that the number of Gaussians in 2DGS [11] is twice than SuperGaussians by modifying the gradient split threshold. "Split" means that the Gaussians is split into twice as many as SuperGaussians at the last split iteration of 2DGS. †indicates that the normal consistency loss is not used.

well as the movable kernel, they still show significant improvements compared to 2DGS [11].
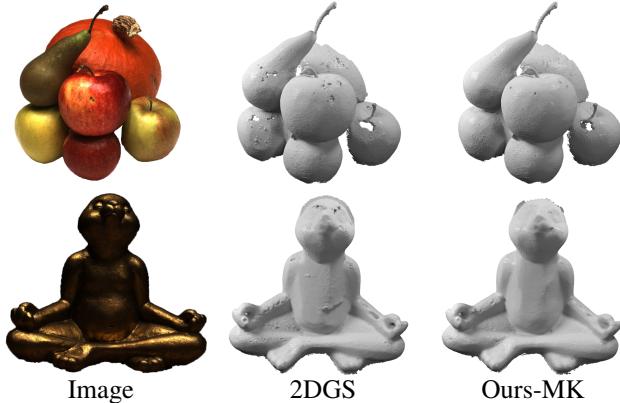

Figure 8. Visual comparison between three different spatially varying functions and 2DGS [11].

Novel View Synthesis. We compare the best setting of SuperGaussians with other state-of-the-art (SoTA) methods. Table 2 shows the PSNR comparison across different datasets. It can be observed that we have achieved optimal or near-optimal results on multiple datasets. Although we do not outperform the original Mip-NeRF360 [3] method on their dataset, we still surpass two explicit Gaussian-based reconstruction methods.

Fig. 6 presents a visual comparison between our results and those of 2DGS [11] on the Synthetic Blender [22] dataset. We provide the error map alongside the ground truth for easier observation. It is evident that 2DGS [11] struggles with reconstructing shape boundaries and abrupt parts. For instance, in the "mic" model, its wires and brackets are not clearly visible from certain angles, whereas our method addresses these issues effectively.

Fig. 7 demonstrates the visual comparison with 2DGS [11] and 3DGS [16], showcasing the powerful expressiveness of SuperGaussians. For example, in the first row, the *bicycle* example highlights our ability to capture finer details. The distant view of the *garden* example in the second row and the *train* in the fourth row emphasize our method's expressiveness of corner cases that appear less common in the training views. Additionally, since our method can express more details, we can reduce the smearing effect, as demonstrated by the *leaves* in the fifth row.

Table 3 shows the comparison results between our method and 2DGS [11] on the DTU [13] dataset. It should be noted that, following 2DGS [11], the DTU [13] dataset does not include a test set, so we only report the metrics on the training set. It can be seen that our method significantly surpasses 2DGS [11].

Geometry Reconstruction. 2DGS [11] has demonstrated impressive capabilities in geometric reconstruction. Since SuperGaussians is implemented based on 2DGS [11], it inherits these excellent geometric reconstruction capabilities, although this is not our primary objective. To evaluate our method, we enable the normal consistency loss from 2DGS [11], which is important for geometry reconstruction. We test our geometric reconstruction ability on the commonly used DTU dataset [13] with different limits on the number of Gaussians, and report the quantitative analysis in Table 4 and visualization results in Fig. 8. The results demonstrate that our geometric reconstruction capabilities are comparable to 2DGS [11] when there is no limit on the number of Gaussians, while also ensuring the highest PSNR, indicating the best image reconstruction quality. Furthermore, when a limited number of Gaussians is used, our powerful expressiveness becomes apparent, greatly outperforming 2DGS [11] in both geometric reconstruction quality and image rendering quality. We present per-scene results and visualization in the supplementary material.

4.3. Ablation Study

Normal Consistency Loss. Since our goal is to improve the novel view reconstruction capability of Gaussian surfels

	PSNR↑	SSIM↑	LPIPS↓	Parameters↓
8 Kernels	34.04	0.970	0.030	105
Sigmoid Kernel	33.97	0.969	0.030	81
Ours-MK	34.10	0.970	0.030	81

Table 7. Ablation of the number of kernels and kernel function forms on the Synthetic Blender dataset [22].

	Training Time (s)↓	FPS↑
2DGS	635.25	210.73
Ours-MK	1083.13	133.25

Table 8. Training cost (seconds) and render cost (FPS) of our method on the Synthetic Blender [22] dataset.

rather than their geometric reconstruction capability, we do not use the normal consistency loss provided by 2DGS [11]. We report the ablation study of this loss in Table 5, where we tested our method and the 2DGS [11] method on the Synthetic Blender dataset [22] both with and without normal consistency loss. All indicators showed that our method is significantly better than the baseline method, regardless of whether normal consistency loss is used.

Comparison with 2DGS. To facilitate a fair comparison with 2DGS [11] and further demonstrate our enhancement of Gaussian expressiveness, we tested our method using the same or fewer parameters as 2DGS [11], as shown in Table 6. As seen in Fig. 4, for each Gaussian, the number of parameters used by SuperGaussians (MK) is about 1.4 times that of the original 2DGS [11]. To avoid the misconception that our advantage lies solely in the number of parameters, we controlled the number of Gaussians in 2DGS [11] to be twice that of SuperGaussians for comparison. When 2DGS [11] uses twice the number of Gaussians, the number of parameters is approximately 1.43 times that of SuperGaussians.

We used two methods to increase the number of points in 2DGS [11] as shown in Table 6. One method was to directly modify the threshold of gradient to allow 2DGS [11] to split and clone more freely ("Grad" in the table). The other method was to split 2DGS [11] into twice the number of SuperGaussians at the final split iteration ("Split" in the table). It can be seen that even when 2DGS [11] uses twice the number of Gaussians as ours, which equates to 1.43 times the number of parameters, its expressiveness is still weaker than ours. This holds true regardless of whether the normal consistency loss is used, demonstrating the powerful scene representation capabilities of our spatially varying function.

Design of Kernels. We conducted ablations on the design of the optimal form of movable kernels in our spatially varying function, as shown in Table 7. In all other experiments,

we use four movable kernels, and we show here how the results change when using eight kernels on the Synthetic Blender dataset [22]. Similarly, we also tried changing the form of the kernel function from an exponential function $\mathcal{F}_{\mathbf{K}_i}$ to a sigmoid function $\mathcal{F}_{\mathbf{S}_i}$:

$$\mathcal{F}_{\mathbf{S}_i}(\mathbf{p}) = 1 - \tanh(\|\mathbf{p} - \mathbf{K}_i\|^2) \qquad (9)$$

where $\tanh(x) = \frac{\sinh(x)}{\cosh(x)}$. Table 7 demonstrates the superiority of our method. Increasing the number of kernels to eight does not significantly improve our results and leads to an increase in the number of parameters. Replacing the kernel function can achieve results close to ours, but still cannot surpass our method.

4.4. Limitations and Future Work

Timing. One of our limitations is the running time. Since we have added spatially varying function calculations in both the forward rendering and back-propagation stages, and have not deeply optimized the code like 2DGS [11], the current training and rendering speeds are slightly slower than 2DGS [11]. Table 8 shows the comparison of our training cost and rendering cost on the Synthetic Blender [22] dataset with 2DGS [11].

More Spatially Varying Functions. Another limitation is that we have not fully explored the potential of spatially varying functions. The design of spatially varying functions can be further studied. Additionally, implementing spatially varying functions on Gaussian ellipsoids [16] is also an interesting research direction.

5. Conclusion

In this paper, we introduce a new method called SuperGaussians that utilizes spatially varying colors and opacity in a single Gaussian primitive to enhance its representation ability. We propose three different spatially varying functions defined on Gaussian primitives, each of which outperforms the baseline 2DGS [11]. Additionally, the movable kernels outperform the current state-of-the-art methods on almost all datasets for novel view synthesis. When using the normal consistency loss, we achieve geometry reconstruction quality comparable to 2DGS [11] and outperform 2DGS [11] when the number of Gaussians is limited, while significantly improving image rendering quality. Although our training and rendering speeds are slower than baseline methods due to code optimization issues, we provide a new direction for further research on Gaussian primitives and make it possible to implement more effective spatial variation functions.

References

[1] Jonathan T Barron, Ben Mildenhall, Matthew Tancik, Peter Hedman, Ricardo Martin-Brualla, and Pratul P Srinivasan. Mip-nerf: A multiscale representation for anti-aliasing neural radiance fields. In *Proceedings of the IEEE/CVF International Conference on Computer Vision*, pages 5855–5864, 2021. 2

[2] Jonathan T Barron, Ben Mildenhall, Dor Verbin, Pratul P Srinivasan, and Peter Hedman. Mip-nerf 360: Unbounded anti-aliased neural radiance fields. In *Proceedings of the IEEE/CVF Conference on Computer Vision and Pattern Recognition*, pages 5470–5479, 2022. 2

[3] Jonathan T Barron, Ben Mildenhall, Dor Verbin, Pratul P Srinivasan, and Peter Hedman. Mip-nerf 360: Unbounded anti-aliased neural radiance fields. In *Proceedings of the IEEE/CVF conference on computer vision and pattern recognition*, pages 5470–5479, 2022. 2, 5, 6, 7, 11, 12, 14

[4] Jonathan T Barron, Ben Mildenhall, Dor Verbin, Pratul P Srinivasan, and Peter Hedman. Zip-nerf: Anti-aliased grid-based neural radiance fields. In *Proceedings of the IEEE/CVF International Conference on Computer Vision*, pages 19697–19705, 2023. 2

[5] Dominique Brunet, Edward R Vrscay, and Zhou Wang. On the mathematical properties of the structural similarity index. *IEEE Transactions on Image Processing*, 21(4):1488–1499, 2011. 5

[6] David Charatan, Sizhe Lester Li, Andrea Tagliasacchi, and Vincent Sitzmann. pixelsplat: 3d gaussian splats from image pairs for scalable generalizable 3d reconstruction. In *Proceedings of the IEEE/CVF Conference on Computer Vision and Pattern Recognition*, pages 19457–19467, 2024. 2

[7] Pinxuan Dai, Jiamin Xu, Wenxiang Xie, Xinguo Liu, Huamin Wang, and Weiwei Xu. High-quality surface reconstruction using gaussian surfels. In *SIGGRAPH 2024 Conference Papers*. Association for Computing Machinery, 2024. 2

[8] Yasutaka Furukawa and Jean Ponce. Accurate, dense, and robust multiview stereopsis. *IEEE Transactions on Pattern Analysis and Machine Intelligence*, 32(8):1362–1376, 2010. 2

[9] Antoine Guédon and Vincent Lepetit. Sugar: Surface-aligned gaussian splatting for efficient 3d mesh reconstruction and high-quality mesh rendering. In *Proceedings of the IEEE/CVF Conference on Computer Vision and Pattern Recognition*, pages 5354–5363, 2024. 2, 12

[10] Abdullah Hamdi, Luke Melas-Kyriazi, Jinjie Mai, Guocheng Qian, Ruoshi Liu, Carl Vondrick, Bernard Ghanem, and Andrea Vedaldi. Ges: Generalized exponential splatting for efficient radiance field rendering. In *Proceedings of the IEEE/CVF Conference on Computer Vision and Pattern Recognition*, pages 19812–19822, 2024. 2

[11] Binbin Huang, Zehao Yu, Anpei Chen, Andreas Geiger, and Shenghua Gao. 2d gaussian splatting for geometrically accurate radiance fields. In *ACM SIGGRAPH 2024 Conference Papers*, pages 1–11, 2024. 1, 2, 3, 4, 5, 6, 7, 8, 11, 12, 13

[12] Yi-Hua Huang, Yan-Pei Cao, Yu-Kun Lai, Ying Shan, and Lin Gao. Nerf-texture: Texture synthesis with neural radiance fields. In *ACM SIGGRAPH 2023 Conference Proceedings*, pages 1–10, 2023. 2

[13] Rasmus Jensen, Anders Dahl, George Vogiatzis, Engin Tola, and Henrik Aanæs. Large scale multi-view stereopsis evaluation. In *Proceedings of the IEEE conference on computer vision and pattern recognition*, pages 406–413, 2014. 2, 5, 7, 11, 12, 13, 17, 18

[14] Artur Kasymov, Bartosz Czekaj, Marcin Mazur, and Przemysław Spurek. Neggs: Negative gaussian splatting. *arXiv preprint arXiv:2405.18163*, 2024. 3

[15] Michael Kazhdan, Matthew Bolitho, and Hugues Hoppe. Poisson surface reconstruction. In *Proceedings of the fourth Eurographics symposium on Geometry processing*, 2006. 2

[16] Bernhard Kerbl, Georgios Kopanas, Thomas Leimkühler, and George Drettakis. 3d gaussian splatting for real-time radiance field rendering. *ACM Trans. Graph.*, 42(4):139–1, 2023. 1, 2, 3, 4, 5, 6, 7, 8, 11, 12

[17] Arno Knapitsch, Jaesik Park, Qian-Yi Zhou, and Vladlen Koltun. Tanks and temples: Benchmarking large-scale scene reconstruction. *ACM Transactions on Graphics (ToG)*, 36 (4):1–13, 2017. 2, 5, 6, 11

[18] Haolin Li, Jinyang Liu, Mario Sznaier, and Octavia Camps. 3d-hgs: 3d half-gaussian splatting. *arXiv preprint arXiv:2406.02720*, 2024. 2, 3

[19] Siyou Lin, Dong Xiao, Zuoqiang Shi, and Bin Wang. Surface reconstruction from point clouds without normals by parametrizing the gauss formula. *ACM Transactions on Graphics*, 42(2):1–19, 2022. 2

[20] Tao Lu, Mulin Yu, Linning Xu, Yuanbo Xiangli, Limin Wang, Dahua Lin, and Bo Dai. Scaffold-gs: Structured 3d gaussians for view-adaptive rendering. In *Proceedings of the IEEE/CVF Conference on Computer Vision and Pattern Recognition*, pages 20654–20664, 2024. 2

[21] Keyang Luo, Tao Guan, Lili Ju, Haipeng Huang, and Yawei Luo. P-mvsnet: Learning patch-wise matching confidence aggregation for multi-view stereo. In *Proceedings of the IEEE/CVF International Conference on Computer Vision*, pages 10452–10461, 2019. 2

[22] Ben Mildenhall, Pratul P Srinivasan, Matthew Tancik, Jonathan T Barron, Ravi Ramamoorthi, and Ren Ng. Nerf: Representing scenes as neural radiance fields for view synthesis. *Communications of the ACM*, 65(1):99–106, 2021. 1, 2, 5, 7, 8, 11, 12, 15, 16

[23] Liangliang Nan and Peter Wonka. Polyfit: Polygonal surface reconstruction from point clouds. In *Proceedings of the IEEE International Conference on Computer Vision*, pages 2353–2361, 2017. 2

[24] OpenMVS. Openmvs: Open multi-view stereo reconstruction library. 2

[25] Johannes L Schonberger and Jan-Michael Frahm. Structure-from-motion revisited. In *Proceedings of the IEEE conference on computer vision and pattern recognition*, pages 4104–4113, 2016. 2

[26] Johannes Lutz Schönberger, Enliang Zheng, Marc Pollefeys, and Jan-Michael Frahm. Pixelwise view selection for unstructured multi-view stereo. In *European Conference on Computer Vision (ECCV)*, 2016. 2

[27] Steven M Seitz, Brian Curless, James Diebel, Daniel Scharstein, and Richard Szeliski. A comparison and evaluation of multi-view stereo reconstruction algorithms. In *2006 IEEE computer society conference on computer vision and pattern recognition (CVPR'06)*, pages 519–528. IEEE, 2006. 2

[28] Peng Wang, Lingjie Liu, Yuan Liu, Christian Theobalt, Taku Komura, and Wenping Wang. Neus: Learning neural implicit surfaces by volume rendering for multi-view reconstruction. *arXiv preprint arXiv:2106.10689*, 2021. 2, 11

[29] Rui Xu, Zixiong Wang, Zhiyang Dou, Chen Zong, Shiqing Xin, Mingyan Jiang, Tao Ju, and Changhe Tu. Rfeps: Reconstructing feature-line equipped polygonal surface. *ACM Transactions on Graphics (TOG)*, 41(6):1–15, 2022. 2

[30] Rui Xu, Zhiyang Dou, Ningna Wang, Shiqing Xin, Shuangmin Chen, Mingyan Jiang, Xiaohu Guo, Wenping Wang, and Changhe Tu. Globally consistent normal orientation for point clouds by regularizing the winding-number field. *ACM Transactions on Graphics (TOG)*, 42(4):1–15, 2023. 2

[31] Yao Yao, Zixin Luo, Shiwei Li, Tian Fang, and Long Quan. Mvsnet: Depth inference for unstructured multi-view stereo. In *Proceedings of the European conference on computer vision (ECCV)*, pages 767–783, 2018. 2

[32] Yao Yao, Zixin Luo, Shiwei Li, Tianwei Shen, Tian Fang, and Long Quan. Recurrent mvsnet for high-resolution multi-view stereo depth inference. In *Proceedings of the IEEE/CVF conference on computer vision and pattern recognition*, pages 5525–5534, 2019. 2

[33] Lior Yariv, Jiatao Gu, Yoni Kasten, and Yaron Lipman. Volume rendering of neural implicit surfaces. *Advances in Neural Information Processing Systems*, 34:4805–4815, 2021. 11

[34] Zehao Yu and Shenghua Gao. Fast-mvsnet: Sparse-to-dense multi-view stereo with learned propagation and gauss-newton refinement. In *Proceedings of the IEEE/CVF conference on computer vision and pattern recognition*, pages 1949–1958, 2020. 2

[35] Zehao Yu, Anpei Chen, Binbin Huang, Torsten Sattler, and Andreas Geiger. Mip-splatting: Alias-free 3d gaussian splatting. In *Proceedings of the IEEE/CVF Conference on Computer Vision and Pattern Recognition*, pages 19447–19456, 2024. 2, 3

[36] Jingyang Zhang, Shiwei Li, Zixin Luo, Tian Fang, and Yao Yao. Vis-mvsnet: Visibility-aware multi-view stereo network. *International Journal of Computer Vision*, 131(1): 199–214, 2023. 2

[37] Richard Zhang, Phillip Isola, Alexei A Efros, Eli Shechtman, and Oliver Wang. The unreasonable effectiveness of deep features as a perceptual metric. In *CVPR*, 2018. 5

[38] Matthias Zwicker, Hanspeter Pfister, Jeroen Van Baar, and Markus Gross. Ewa volume splatting. In *Proceedings Visualization, 2001. VIS'01.*, pages 29–538. IEEE, 2001. 3

A. Implementation Details

Following 2DGS [11] and 3DGS [16], we tested the Synthetic Blender dataset [22] and Tanks&Temples [17] at their native resolution. We tested the DTU [13] dataset at a resolution of $0.8K \times 0.6K$, which is one quarter of the native resolution. For the Mip-NeRF360 [3] dataset, we followed the 2DGS [11] test settings, using the "images_4" setting for outdoor scenes, which has a resolution of about $0.8K \times 0.6K$, and the "images_2" setting for indoor scenes, which has a resolution of about $1.0K \times 0.8K$. The pictures and quantitative data (except DTU [13]) we show are calculated and rendered on the test set, which never appeared in the training set.

B. Detailed Tables

	Mic	Chair	Ship	Materials	Lego	Drums	Ficus	Hotdog	Mean
2DGS	33.66	35.11	31.34	30.17	34.75	24.99	35.83	37.13	32.87
Ours-BI	36.16	35.32	31.64	30.23	35.80	26.33	36.20	37.86	33.69
Ours-NN	35.68	34.75	31.36	29.99	35.37	26.22	35.96	37.77	33.39
Ours-MK	36.43	36.17	31.97	30.54	36.49	26.41	36.57	38.24	34.10

Table 9. Comparison of three different spatial variation functions and the original 2DGS [11] without spatial variation function. This table showing the PSNR on Synthetic Blender dataset [22].

	bicycle	flowers	garden	stump	treehill	room	counter	kitchen	bonsai	Mean
2DGS	24.72	21.14	26.65	26.30	22.35	30.91	28.11	30.28	31.29	26.86
Ours-BI	24.67	21.29	26.82	26.18	22.20	29.32	28.78	30.13	31.36	26.75
Ours-NN	24.65	21.15	26.74	26.46	22.27	30.77	28.37	30.45	31.46	26.92
Ours-MK	25.21	21.66	27.20	26.70	22.35	31.05	29.03	30.42	32.17	27.31

Table 10. Comparison of three different spatial variation functions and the original 2DGS without spatial variation function. This table showing the PSNR on Mip-NeRF360 [3].

	Truck	Train	Mean
2DGS	25.12	21.26	23.19
Ours-BI	25.49	22.01	23.75
Ours-NN	25.18	21.34	23.26
Ours-MK	25.66	21.78	23.72

Table 11. Comparison of three different spatial variation functions and the original 2DGS without spatial variation function. This table showing the PSNR on Tanks&Temples [17] dataset.

We first provide detailed versions of the corresponding tables in the main text. We present the comparison of three different spatial variation functions on the Synthetic Blender [22], Mip-NeRF360 [3], and Tanks&Temples [17] datasets against the baseline method 2DGS [11] in Table 9, Table 10, and Table 11. A simplified version that only provides the mean values can be found in Table 1 in the main text. It is worth noting that the three tables here show the final PSNR values without limiting the number of Gaussians.

Next, we present a detailed comparison of our best setting (movable kernels) with several existing state-of-the-art methods. Table 12, Table 13, and Table 14 show

	Mic	Chair	Ship	Materials	Lego	Drums	Ficus	Hotdog	Mean
Plenoxels	33.26	33.98	29.62	29.14	34.10	25.35	31.83	36.81	31.76
INGP-Base	36.22	35.00	31.10	29.78	36.39	26.02	33.51	37.40	33.18
Mip-NeRF	36.51	35.14	30.41	30.71	35.70	25.48	33.29	37.48	33.09
Point-NeRF	35.95	35.40	30.97	29.61	35.04	26.06	36.13	37.30	33.30
3DGS	35.36	35.83	30.80	30.00	35.78	26.15	34.87	37.72	33.32
2DGS	33.66	35.11	31.34	30.17	34.75	24.99	35.83	37.13	32.87
Ours-MK	36.43	36.17	31.97	30.54	36.49	26.41	36.57	38.24	34.10

Table 12. PSNR on Synthetic Blender dataset [22]. Note that all data except 2DGS are from the 3DGS paper.

	bicycle	flowers	garden	stump	treehill	room	counter	kitchen	bonsai	Mean
Plenoxels	21.91	20.10	23.49	20.66	22.25	27.59	23.62	23.42	24.67	23.08
INGP-Base	22.19	20.35	24.60	23.63	22.36	29.27	26.44	28.55	30.34	25.30
INGP-Big	22.17	20.65	25.07	23.47	22.37	29.69	26.69	29.48	30.69	25.59
Mip-NeRF360	24.37	21.73	26.98	26.40	22.87	31.63	29.55	32.23	33.46	27.69
3DGS	25.25	21.52	27.41	26.55	22.49	30.63	28.70	30.32	31.98	27.21
2DGS	24.72	21.14	26.65	26.30	22.35	30.91	28.11	30.28	31.29	26.86
Ours_MK	25.21	21.66	27.20	26.70	22.35	31.05	29.03	30.42	32.17	27.31

Table 13. PSNR on Mip-NeRF360 [3]. Note that all data except 2DGS are from the 3DGS paper.

	Truck	Train
Plenoxels	23.221	18.927
INGP-Base	23.260	20.170
INGP-Big	23.383	20.456
Mip-NeRF360	24.912	19.523
3DGS	25.187	21.097
2DGS	25.12	21.26
Ours-MK	25.66	21.78

Table 14. PSNR on Tanks&Temples [17] dataset. Note that all data except 2DGS are from the 3DGS paper.
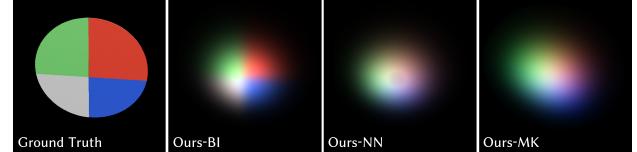

Figure 9. Here we demonstrate the capabilities of three different spatially varying functions on a single Gaussian. Bilinear interpolation is able to fit the abrupt changes better, but causes the gradient to vanish in other regions.

the comparison between our method and existing methods on the Synthetic Blender [22], Mip-NeRF360 [3], and Tanks&Temples [17] datasets, respectively. It can be seen that we surpass the existing methods except on the Mip-NeRF360 [3] dataset. On the Mip-NeRF360 dataset, we also surpass all explicit Gaussian-based methods. A summarized version of these three tables can be found in Table 2 in the main text.

C. Geometry Reconstruction

In this section, we present a detailed comparison of geometric reconstruction on the DTU [13] dataset. Table 15 compares our reconstruction results with other existing methods without Gaussian number restrictions. The methods compared include implicit methods such as NeRF [22], VolSDF [33], and NeuS [28], as well as explicit methods

such as 3DGS [16], SuGaR [9], 2DGS [11], and Super-Gaussians. We also provide the PSNR of image quality in the last column. All data, except for ours and 2DGS, are sourced from the 2DGS [11] paper. The normal consistency loss from 2DGS [11] is used in this table. Tables 16 and 17 further compare our geometric reconstruction with 2DGS when the number of Gaussians is limited to 50K and 100K. More visualization results are shown in Fig. 10. It can be observed that SuperGaussians has a clear advantage over 2DGS under a limited number of Gaussians.

D. Discussion on Spatially Varying Functions

Fig. 9 demonstrates the image fitting capabilities of three spatial variation functions on a single Gaussian. We observe that although bilinear interpolation can better fit color mutations, it suffers from the problem of gradient vanishing in other areas. This issue arises because bilinear interpolation requires coordinates within a certain range $(0, 1)$. Therefore, we need to use the sigmoid function in Eq. 5 to scale the (u, v) coordinates before using them. This scaling causes the gradient of a pixel to be almost zero when it falls near the center of a quadrant, making it difficult to perfectly fit the scene.

While the tiny neural network and movable kernel methods cannot fit the color mutations in the original image as precisely, they provide a smooth transition of color without causing the gradient to vanish. Consequently, when multiple Gaussians are superimposed through alpha-blending, these methods exhibit stronger expressiveness.

It is worth noting that for the proposed movable kernels, the kernel position moves with the gradient. In some extreme cases, the kernel center may move outside the Gaussian. At this point, SuperGaussians will degenerate into 2DGS [11]. We do not impose any special restrictions on the kernel position to prevent it from moving outside the Gaussian, as this rarely occurs. In Table 18, we present the probability of the kernel remaining inside the Gaussian across several datasets we tested. It can be seen that there is almost no instance where the kernel moves outside the Gaussian with the gradient.

E. More Results

In this section, we present additional rendering results. Fig. 11 shows the novel view rendering results on the Mip-NeRF360 [3] dataset. Fig. 12 and Fig. 13 display the novel view rendering results on the Synthetic Blender [22] dataset. Finally, we present more rendering results of the DTU [13] dataset at four fixed viewpoints in Fig. 14 and Fig. 15. Note that only the images from the DTU [13] dataset may have appeared in the training set, as we followed the training scripts of 2DGS [11].

	24	37	40	55	63	65	69	83	97	105	106	110	114	118	122	Mean	PSNR↑
NeRF	1.90	1.60	1.85	0.58	2.28	1.27	1.47	1.67	2.05	1.07	0.88	2.53	1.06	1.15	0.96	1.49	30.65
VolSDF	1.14	1.26	0.81	0.49	1.25	0.70	0.72	1.29	1.18	0.70	0.66	1.08	0.42	0.61	0.55	0.86	30.38
NeuS	1.00	1.37	0.93	0.43	1.10	0.65	0.57	1.48	1.09	0.83	0.52	1.20	0.35	0.49	0.54	0.84	31.97
3DGS	2.14	1.53	2.08	1.68	3.49	2.21	1.43	2.07	2.22	1.75	1.79	2.55	1.53	1.52	1.50	1.96	35.76
SuGaR	1.47	1.33	1.13	0.61	2.25	1.71	1.15	1.63	1.62	1.07	0.79	2.45	0.98	0.88	0.79	1.33	34.57
2DGS(P)	0.48	0.91	0.39	0.39	1.01	0.83	0.81	1.36	1.27	0.76	0.70	1.40	0.40	0.76	0.52	0.80	34.52
2DGS	0.45	0.81	0.33	0.38	0.97	0.87	0.78	1.27	1.24	0.67	0.68	1.32	0.38	0.66	0.47	0.75	34.43
Ours	0.44	0.76	0.39	0.39	0.89	0.94	0.74	1.36	1.26	0.77	0.72	1.06	0.38	0.89	0.47	0.76	35.22

Table 15. Chamfer distance and PSNR comparison of geometric reconstruction on the DTU [13] dataset without Gaussian number limitation. Note that all data except ours and 2DGS are from the 2DGS [11] paper, 2DGS(P) is result copied from original paper, and 2DGS is the results of their latest code. and we use the normal consistency loss provided by 2DGS [11] in this table.

	24	37	40	55	63	65	69	83	97	105	106	110	114	118	122	Mean	PSNR↑
2DGS	1.07	1.58	1.90	0.54	1.12	0.89	0.98	1.28	1.56	0.69	1.43	1.54	0.71	0.81	0.57	1.11	28.76
Ours	0.83	1.10	0.77	0.48	0.86	0.99	0.98	1.31	1.49	0.78	1.59	1.52	0.58	1.01	0.59	0.99	29.86

Table 16. Chamfer distance comparison of geometric reconstruction on the DTU [13] dataset under the 50K point limit. We use the normal consistency loss provided by 2DGS [11] in this table.

	24	37	40	55	63	65	69	83	97	105	106	110	114	118	122	Mean	PSNR↑
2DGS	0.83	1.02	0.73	0.42	1.02	0.86	0.81	1.28	1.23	0.68	0.70	1.49	0.39	0.67	0.46	0.84	32.25
Ours	0.57	0.94	0.51	0.40	0.86	1.00	0.84	1.34	1.14	0.77	0.87	1.13	0.41	0.98	0.50	0.82	32.80

Table 17. Chamfer distance comparison of geometric reconstruction on the DTU [13] dataset under the 100K point limit. We use the normal consistency loss provided by 2DGS [11] in this table.

	Synthetic Blender	Mip-NeRF360	Tanks&Temples	DTU
Internal	99.95%	99.60%	99.92%	99.57%

Table 18. Average percentage of kernels falling inside the Gaussian across multiple datasets.
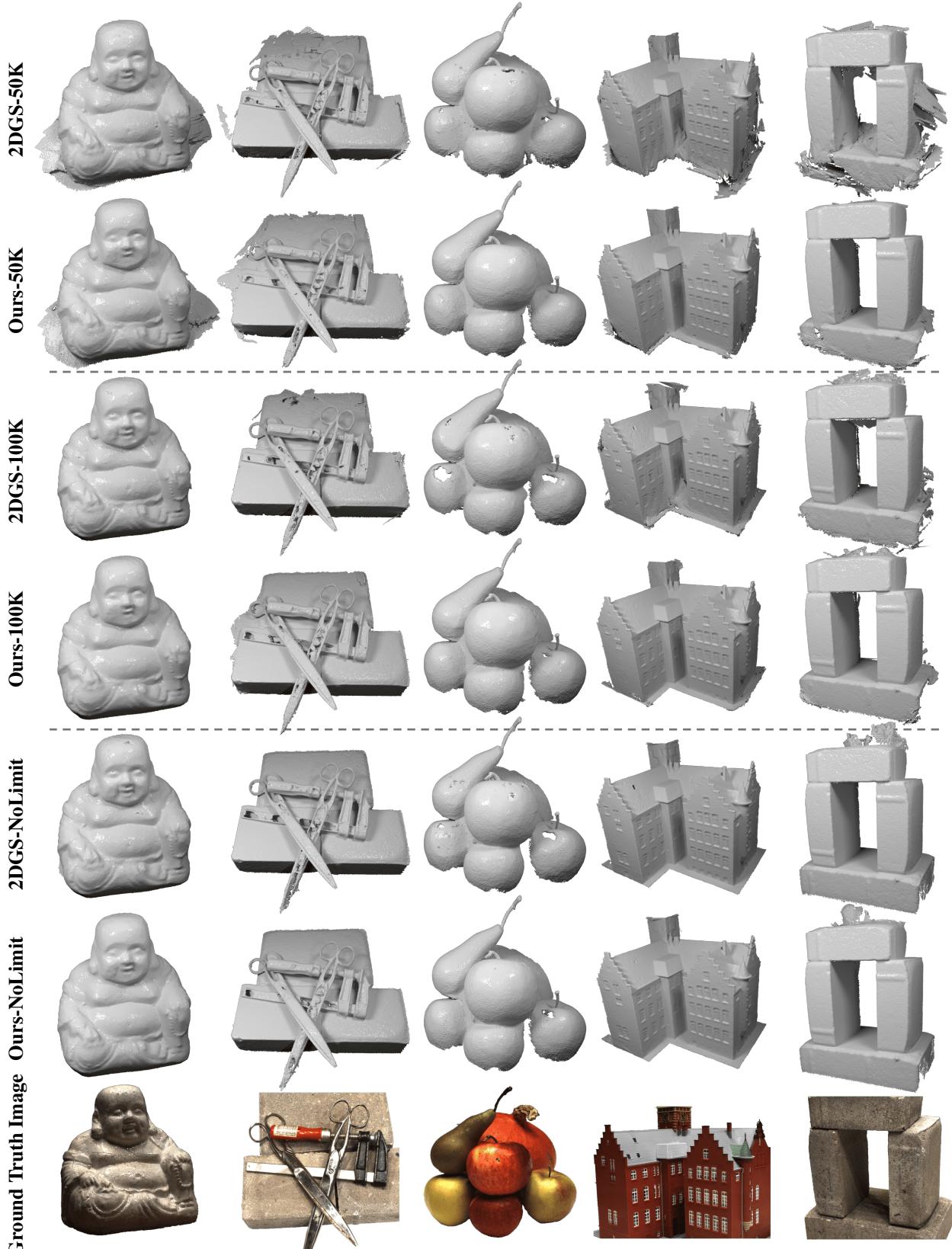
Figure 10. More geometric reconstruction results on the DTU [13] dataset. We show the comparison between 2DGS [11] and our method under different Gaussian number limitations.
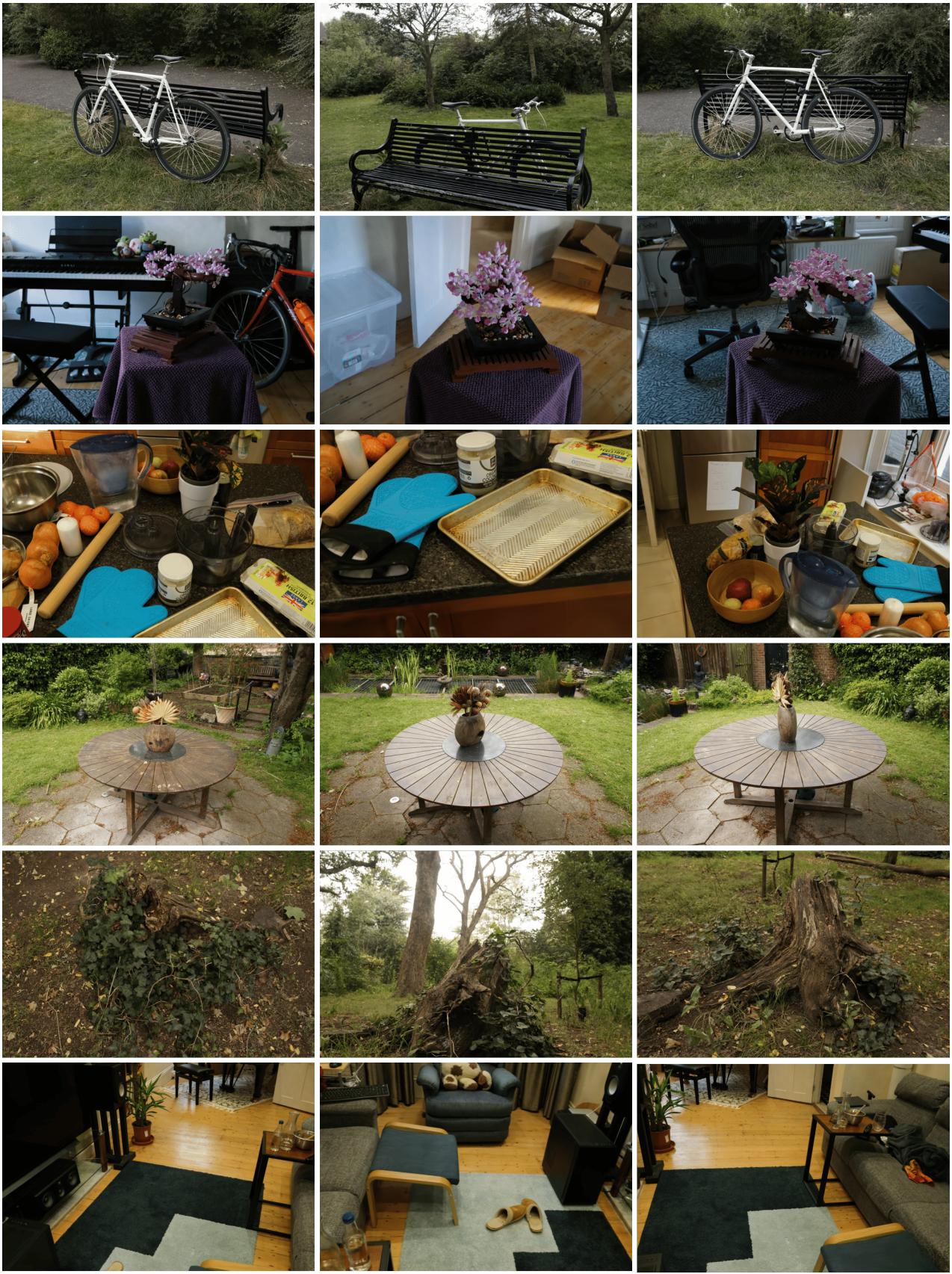
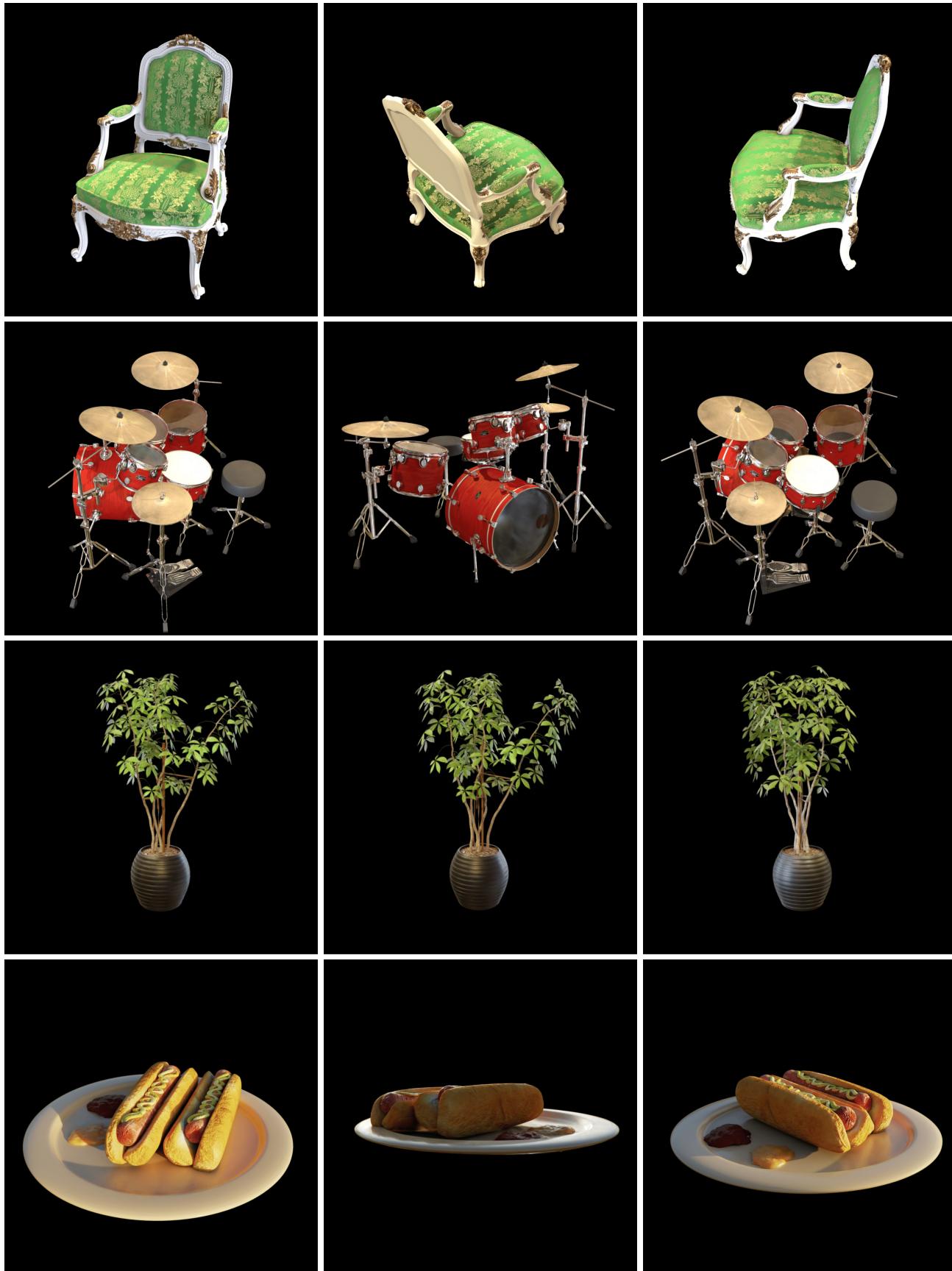Figure 11. Here we show more novel view results of SuperGaussians on the Mip-NeRF360 [3] dataset.

Figure 12. Here we show more novel view results of SuperGaussians on the first part of Synthetic Blender [22] dataset.
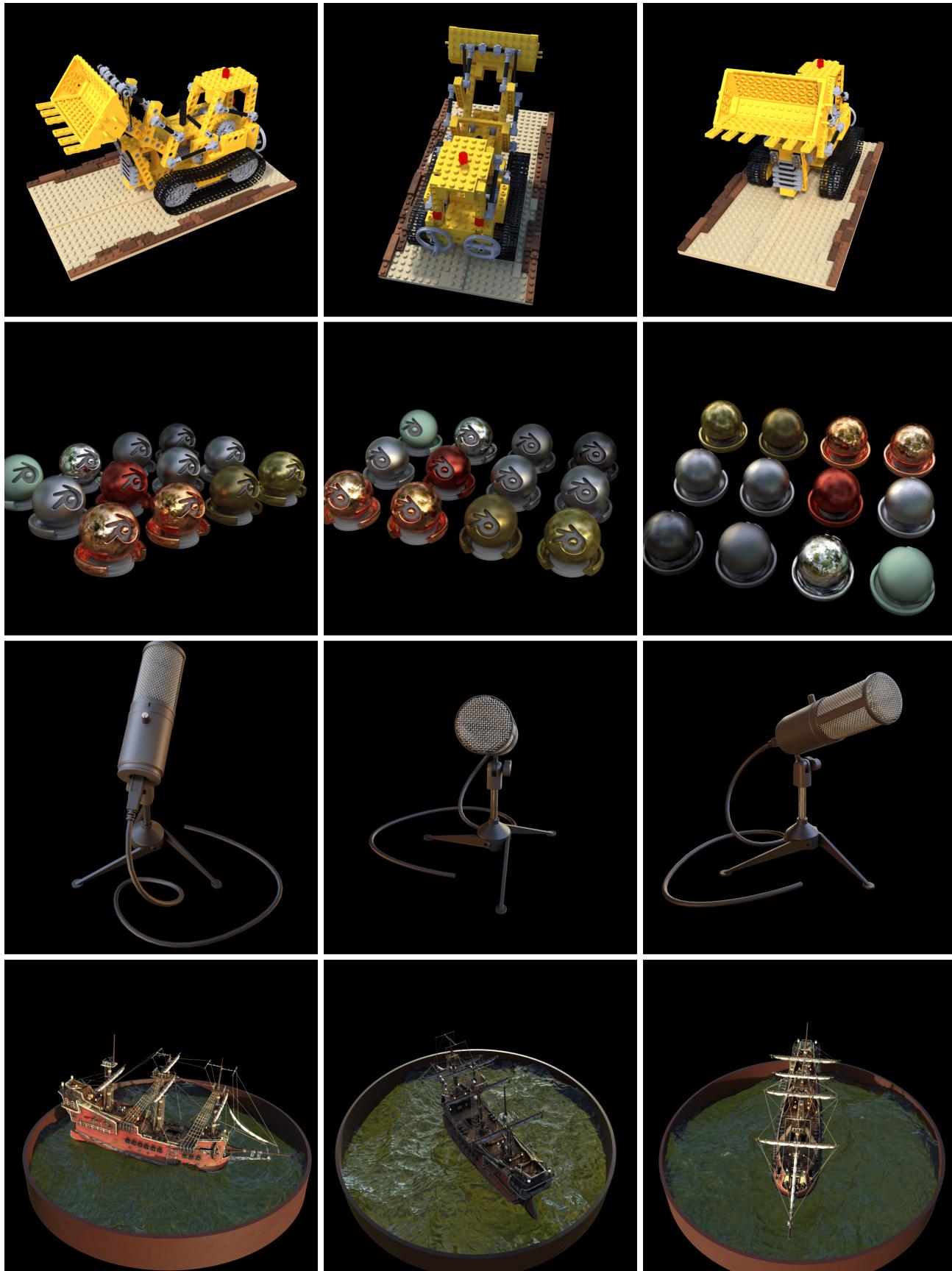
15

Figure 13. Here we show more novel view results of SuperGaussians on the second part of Synthetic Blender [22] dataset.
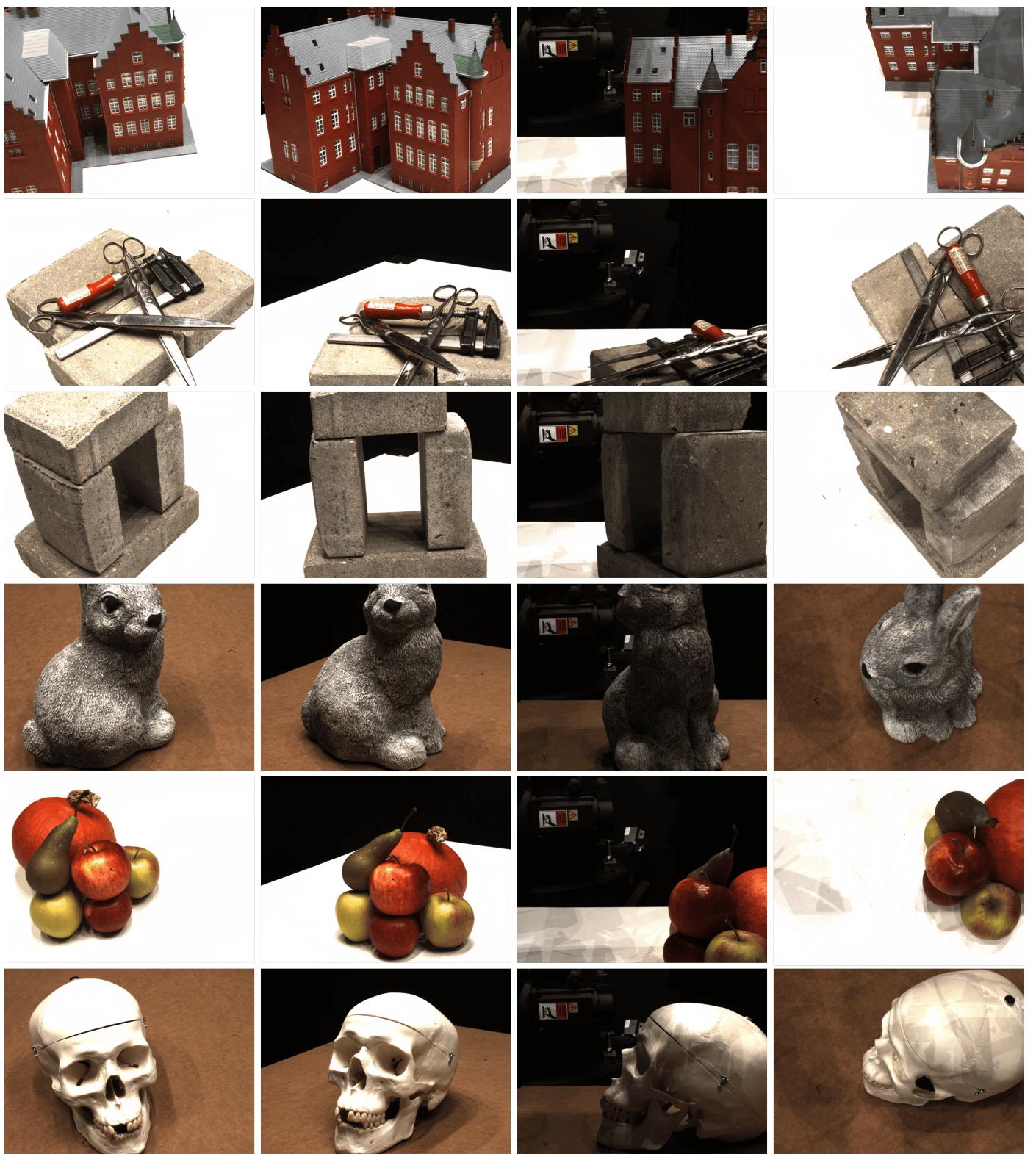
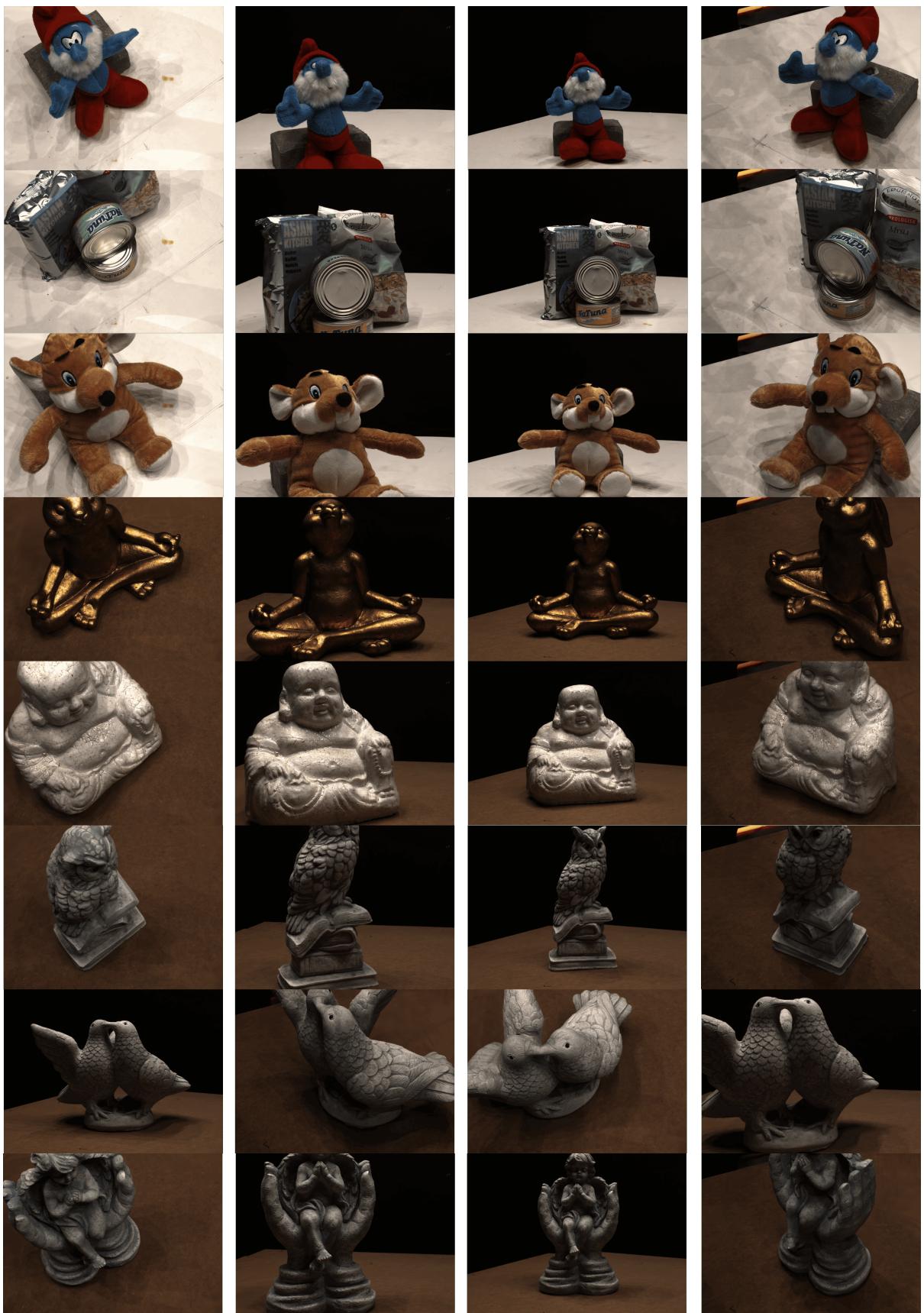Figure 14. Here we show more rendering results of SuperGaussians on the first part of DTU [13] dataset.

Figure 15. Here we show more rendering results of SuperGaussians on the second part of DTU [13] dataset.